

Thermal structure and heat loss at the summit crater of an active lava dome

Steve T. Sahetapy-Engel · Andrew J. L. Harris

Received: 16 May 2007 / Accepted: 13 February 2008 / Published online: 26 March 2008
© Springer-Verlag 2008

Abstract Forward-Looking Infrared (FLIR) nighttime thermal images were used to extract the thermal and morphological properties for the surface of a blocky-to-rubblery lava mass active within the summit crater of the Caliente vent at Santiaguito lava dome (Guatemala). Thermally the crater was characterized by three concentric regions: a hot outer annulus of loose fine material at 150–400°C, an inner cold annulus of blocky lava at 40–80°C, and a warm central core at 100–200°C comprising younger, hotter lava. Intermittent explosions resulted in thermal renewal of some surfaces, mostly across the outer annulus where loose, fine, fill material was ejected to expose hotter, underlying, material. Surface heat flux densities (radiative + free convection) were dominated by losses from the outer annulus ($0.3\text{--}1.5 \times 10^4 \text{ s}^{-1}\text{m}^{-2}$), followed by the hot central core ($0.1\text{--}0.4 \times 10^4 \text{ J s}^{-1}\text{m}^{-2}$) and cold annulus ($0.04\text{--}0.1 \times 10^4 \text{ J s}^{-1}\text{m}^{-2}$). Overall surface power output was also dominated by the outer annulus region ($31\text{--}176 \text{ MJ s}^{-1}$), but the cold annulus contributed equal power ($2.41\text{--}7.07 \text{ MJ s}^{-1}$) as the hot central core ($2.68\text{--}6.92 \text{ MJ s}^{-1}$) due to its greater area. Cooled surfaces (i.e. the upper thermal boundary layer separating surface temperatures from underlying material at magmatic temperatures) across the central core and cold annulus had estimated thicknesses, based on simple conductive model, of 0.3–2.2 and 1.5–4.3 m. The stability of the thermal structure through time and between explosions indicates that it is linked to a deeper structural control likely comprising a central

massive plug, feeding lava flow from the SW rim of the crater, surrounded by an arcuate, marginal fracture zone through which heat and mass can preferentially flow.

Keywords Lava dome · Active vent · Ash plume · Santiaguito · Thermal structures · Plug and shear zones

Introduction

The 1902 eruption of Santa María volcano (Guatemala) was one of the largest explosive eruptions of the twentieth century. During a 36-h period, 7.5 km^3 of dacite was erupted to feed an eruption column that reached a height of at least 28 km (Williams and Self 1983; Rose 1972). The eruption also removed a significant portion of the southern flank of Santa María forming a crater on its southeastern flank (Fig. 1a). Twenty years of repose ensued until June 1922 when a new lava dome, designated as Santiaguito, emerged within the 1902 crater (Sapper 1926; Rose 1972). Eight decades of persistent extrusion of dacite at a time-averaged rate (over the period 1922–2000) of $0.44 \text{ m}^3 \text{ s}^{-1}$ built the 1.1 km^3 Santiaguito lava dome complex with four main centers: El Caliente, El Brujo, La Mitad, El Monje (Rose 1987; Harris et al. 2003). The locus of activity since 1977 has been at the Caliente vent atop the dome unit of the same name. This is considered to be the principal vent of Santiaguito, given its location coincident with the approximate location of the main conduit (Rose 1972, 1987). The latest (and ongoing) activity at Caliente is characterized by high extrusion rates (relative to documented eruption rates at Santiaguito) of $\sim 0.5 \text{ m}^3 \text{ s}^{-1}$ (Harris et al. 2003) and extrusion of extremely well insulated silicic lava which have attained lengths of $\sim 3.9 \text{ km}$ (Harris et al. 2002, 2004). This extrusive activity has been accompanied by intermit-

Editorial responsibility: J Stix

S. T. Sahetapy-Engel (✉) · A. J. L. Harris
HIGP/SOEST, University of Hawaii,
1680 East-West Road,
Honolulu, HI 96822, USA
e-mail: sahetapy@higp.hawaii.edu

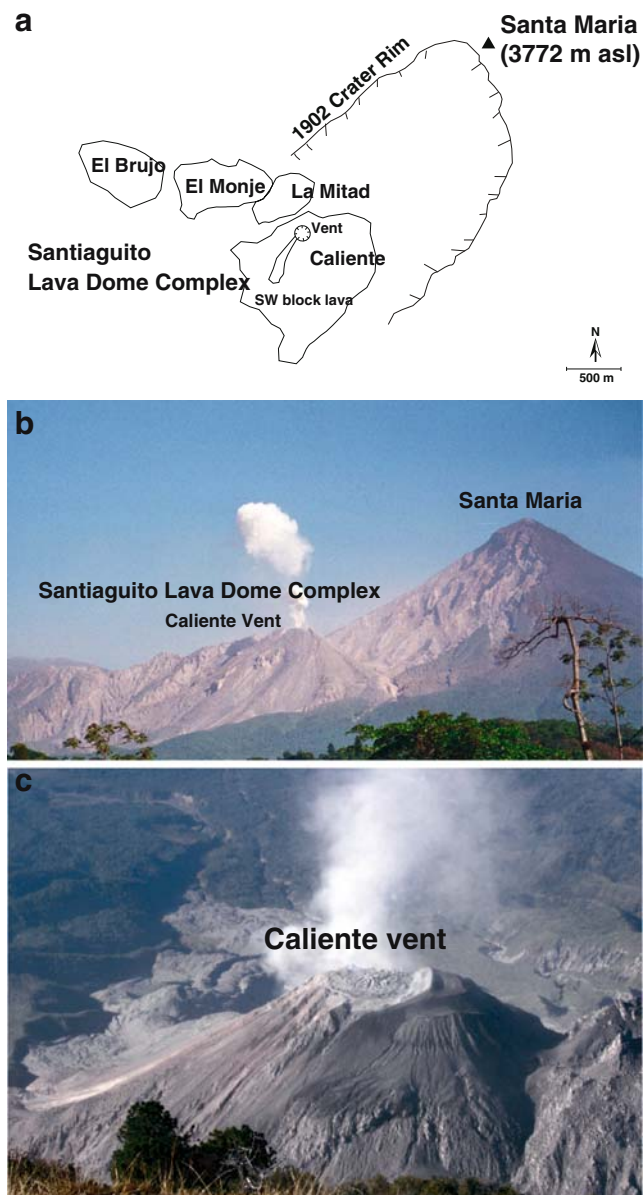


Fig. 1 **a** Sketch map showing the main units of the Santiaguito dome complex and their location within the 1902 explosion crater of Santa Maria. **b** View of Santa Maria volcano and the Santiaguito Lava Dome Complex growing within the crater of the 1902 Santa Maria plinian eruption. View is from the east. Height difference between the Caliente and Santa Maria summits is 1223 m. **c** View of Caliente dome and its summit crater from the top of Santa Maria volcano. The crater vent diameter is approximately 180 m

tent low to moderate intensity explosions producing vertical ash plumes up to 2 km high (Rose 1987; Bluth and Rose 2004; Sahetapy-Engel et al. 2004, 2008; Johnson et al. 2004). These occur from the summit vent at a typical frequency of 1.7 explosions per hour (Sahetapy-Engel et al. 2008).

The location of Santiaguito within the 1902 crater of Santa María is advantageous for observing and measuring

vent activity, where an unobstructed view of the Caliente vent (2,520 m asl) is possible from the summit of Santa María volcano (3,752 m asl). This vantage point is 1,220 m vertically above, and 2,500 m horizontally away from the vent, giving a line of sight view of 2,780 m (Fig. 1). Using digital video footage obtained from this vantage point Bluth and Rose (2004) proposed a hypothetical conduit model at Santiaguito where a dacite plug is rising through a conduit 50 m in diameter. Based on the work of Gonnermann and Manga (2003), Bluth and Rose (2004) further proposed that shear-induced magma fragmentation at the conduit boundaries gave rise to the ash eruptions. Based on integrated thermal and infrasonic observations, Sahetapy-Engel et al. (2008) agreed with shear-induced fragmentation as a likely source; with ash eruptions caused by a rising dacite plug undergoing intermittent stick-slip at the conduit boundaries. They further constrained the depth of fragmentation, this extending over the thickness of the slipping plug, i.e., within a region 100 to 600 m below the crater surface.

Attempts to use field-based thermal infrared remote sensing to describe the surface thermal structure at Santiaguito were first conducted by Birnie (1973) during 1969–1970 using a radiation thermometer. Birnie (1973) recorded maximum surface temperatures, corrected for emissivity and atmospheric effects, of 20–30°C located at the Caliente summit crater, the summit of El Brujo dome (which was actively extruding at the time of measurement) and areas corresponding to fumarolic activity. Birnie (1973) calculated excess radiant heat flow and estimated that the depth to molten rock at El Brujo was 11 m. Sahetapy-Engel et al. (2004) used a combination of single-channel IR thermometer and spectroradiometer data to establish the thermal structure of the Caliente summit crater and its temporal evolution during 2002. Using a two-component thermal mixture model they reported that the summit can be characterized by a 120–250°C surface broken by fractures radiating at high temperatures (>900°C). Thermal renewal of the surface occurs following an explosion where the thermal structure changes from a two-component surface to an isothermal surface radiating at 350–500°C. Here we explore the spatial and temporal features of this surface, and its relation to the inferred plug-like ascent of the magma to feed ash plume emissions and a southward extending block lava flow.

Thermal video camera and data acquisition

The thermal video camera used in this study was a Forward Looking InfraRed (FLIR) ThermoCAM™ P40 model, manufactured by FLIR™ Systems. This camera operates in the 7.5–13 micron spectral range using a focal plane array of uncooled microbolometer detectors, producing a

320×240 pixel calibrated thermal image. The camera has an optical system with a field of view (FOV) of 1.3 mrad. The actual pixel width in the acquired image varies with distance from the instrument to the target (d), and can be calculated from $2d \tan(1.3 \text{ mrad}/2)$. Over our 2,805 m line of sight, this gives a pixel width of 3.6 m, yielding thermal images approximately 1,150×860 m in dimension. The instrument has the capability to perform automatic corrections to take into account surface emissivity and atmospheric effects using a LOWTRAN atmospheric model and user-specified variables for target emissivity, path length (distance from sensor to target), relative humidity and ambient temperature. Collected images can either be stored to a removable CompactFlash™ media card, the instrument's limited onboard memory or, for streaming image acquisition at 15 to 30 images per second, by connection to a laptop via Firewire™.

We collected thermal images of the summit vent of Santiaguito's Caliente dome unit during the early morning of January 16th, 2005, from the summit of Santa María. Thermal images were acquired at a rate of 30 images per second between 2:52 A.M. and 6:38 A.M. (all times are local), where nighttime imaging minimized the effects of solar heating on recorded surface temperatures. This also took advantage of the clear viewing conditions of the early morning, which typically only last until around 10 A.M. during the dry season. Relative humidity and ambient temperature were measured in-situ at 15-min intervals and input to allow atmospheric correction. For emissivity correction we used a value of 0.9 following Birnie (1973). In addition, 52 images were collected after sunrise (between 7 and 8 A.M.) at random intervals to observe certain eruptive phenomena and surface structures. Digital photos at 3 to 5 megapixel resolution were also collected to facilitate comparison with the thermal data.

The accuracy of the instrument is $\pm 2^\circ\text{C}$, or 2% of the reading, whichever is greater. This corresponds to an error of 2 to 10°C given the range of temperatures (< 40 to 520°C) recorded during the observation. The oblique viewing angle of the crater from Santa María summit introduced distortion of pixel area as well as decreasing emissivity with increasing viewing angle from normal (Ball and Pinkerton 2006). The viewing angle from Santa María summit to the Caliente crater is approximately 63°, which correspond to temperature errors of between 14–20°C. We corrected the FLIR data for atmospheric attenuation by feeding measured relative humidity, ambient temperature and distance to target into the instrument's built-in correction algorithm. This correction assumes that relative humidity and ambient temperature, which is limited to at-camera measurement, is constant along the path length from the camera to the target; an assumption which may not be realistic.

A total of six explosions producing vertical ash plumes occurred during the nighttime acquisition period. Measured atmospheric parameters (used to correct the thermal images) for each explosion are shown in Table 1. Only the first four explosions have good quality images and are used for analysis. During the last two explosions, relative humidity levels reached values of >90%, culminating in condensation forming on the camera lens. The recorded images are very poor in quality, with anomalously low temperatures, and are thus omitted from any quantitative analysis.

Surface thermal distribution

Thermal mapping

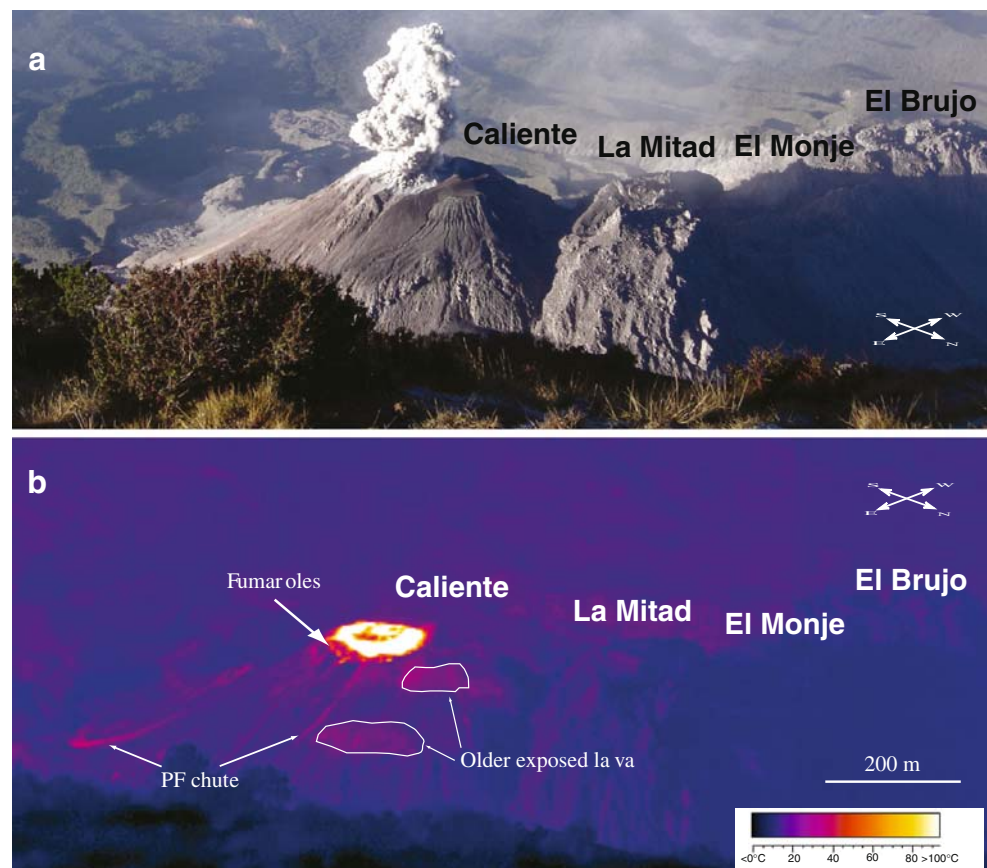
A panoramic view of the four lava dome units that comprise the Santiaguito dome complex can be obtained from the summit of Santa María (Fig. 2). The mosaic was constructed using three FLIR daytime images, and compared with the corresponding digital photo mosaic. The thermal image mosaic confirms that current thermal activity at Santiaguito is strictly confined to the Caliente vent, with no significant thermal anomalies being detected elsewhere. On the Caliente dome itself, the main thermal feature is located within the summit crater. However, two additional thermal anomalies are also present on the flank of the dome. The first is evident on the upper flank, immediately outside of the summit crater, and comprises a ring of relatively hot material that appear to be radiating at elevated temperatures of 60–100°C, most likely due to emplacement of warm deposits from ash plumes and the presence of fumaroles. Previous workers have observed the presence of fumarolic activity on the upper flank of the Caliente, near the summit crater (e.g. Stoiber and Rose 1969; Sahetapy-Engel et al. 2004). Stoiber and Rose (1969) measured fumarole temperatures near the Caliente vent as high as 700°C but decreasing to 300°C only ~0.9 m away from the

Table 1 Atmospheric parameters for the six explosions recorded during the observation period

Eruption no.	Time	RH percent	T_{atm} °C
1	3:06:48 A.M.	73	4.4
2	3:22:18 A.M.	75	4.1
3	3:58:20 A.M.	87	7.5
4	4:23:23 A.M.	85	4.3
5	5:59:50 A.M.	91	1.7
6	6:06:11 A.M.	98	3.2

Time of explosion is estimated from initial time of plume exit from the vent. Relative humidity (RH) and ambient temperature (T_{atm}) are both measured at the observation site during each explosion.

Fig. 2 **a** Panoramic view of the four lava dome units comprising the Santiaguito lava dome complex taken from Santa Maria summit showing a vertical ash plume emitted from Caliente vent. The distance from Caliente to Brujo is approximately 1.5 km. **b** A composite of three FLIR thermal images of the same view showing the main flank and summit crater thermal anomalies of the Caliente in January 2004



fumarole vent. These fumaroles would be sub-pixel features in pixel sizes relevant to this study. Thus the pixel-integrated temperature would be somewhat lower than that of the vent residing within the pixel. The second flank anomaly is located on the left hand side of the image, where an elongate feature is radiating at temperatures of 30 to 40°C. The location of the feature corresponds to one of the main paths followed by small pyroclastic flows accompanying the vertical ash eruptions. The anomaly is thus most likely comprised of warm, cooling, pyroclastic flow deposits. During daytime periods this feature may not be thermally distinguishable, as the heat from the sun warms the surrounding dome surface to a similar temperature range (Harris et al. 2002).

A thermal image focused on the summit crater of Caliente collected at sunrise is compared with corresponding digital photo in Fig. 3. From this we can distinguish three different thermal zones within the summit vent area. These three zones are concentrically arranged and comprise (1) an outer annulus of relatively high temperatures, (2) an inner annulus that is relatively cool, and (3) a central core at intermediate to high temperatures. Warm pyroclastic deposits from intermittent ash eruptions are visible on the inner crater wall in the right-hand side of the summit as well as on the upper flanks of the dome on the left-hand side of the vent.

Temperature profile extracted along a horizontal cross-section across the summit (marked L–L' on Fig. 4) shows the three thermal regions in the horizontal plane. The hot outer annulus is represented by the two outer peaks in the profile, with peak temperatures ranging from 175 to 225°C. The cool inner annulus is represented by the two temperature troughs, with temperatures as low as 80°C. The central temperature peak in the profile represents the central core region, with temperatures of up to 150°C. We measured the dimensions of these thermal regions using this horizontal profile because, being orientated at right angles to the line of sight, it provides the smallest viewing angle errors. The maximum width of the outer annulus is approximately 10 pixels or 36 m. The maximum width for the inner annulus is 11 pixels or 40 m, and the central core has a diameter of approximately 10 pixels or 36 m. The inner annulus is horseshoe-like in shape, with a discontinuity on the back side (southwest portion) of the crater. The surface within the discontinuity has temperatures similar to those of the hot central core, effectively extending the hot central core region out towards the crater rim in that portion of the crater. The location of this discontinuity corresponds to the location from which an active block lava flow was being emplaced onto the southwest flank of the dome (SW block lava flow, Fig. 1). The thermal image (Fig. 3) also

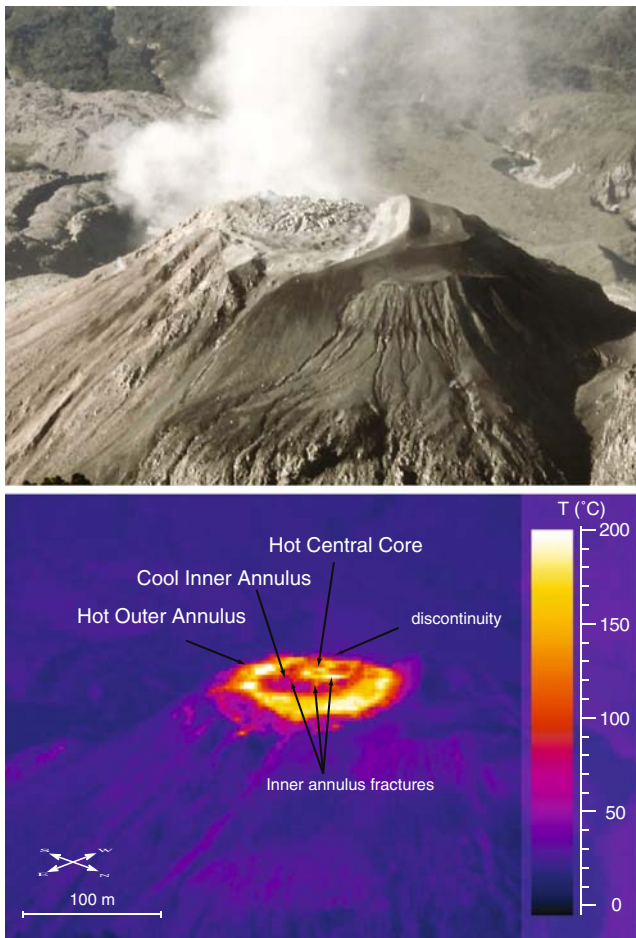


Fig. 3 Digital photo and co-located thermal image of the Caliente dome and its summit crater. The thermal image shows the three-zone thermal structure within the summit crater comprising an outer hot annulus, a cool inner annulus and a hot central core

shows the presence of one pixel-wide (3.6 m-wide) linear hot features cross-cutting the inner annulus. These features appear to be fractures dissecting the inner annulus, with temperatures between 120 to 200°C.

Temporal stability of thermal structures

Intermittent explosions from the summit vent produced changes in temperature, or thermal renewal, of the surface, thereby disrupting simple cooling of the surface and setting up a cyclic (cooling and heating) thermal phenomenon that was first observed by Sahetapy-Engel et al. (2004). Six explosions were captured during the nighttime portion of our dataset, allowing improved observation of the effect the explosions on the vent thermal structure. Sequences of FLIR images from the first four explosions are shown in Figs. 5 and 6. Temperature values are most likely the most accurate for explosions 1 and 2 (Fig. 5), given lower humidity levels at those times (Table 1). The FLIR images collected during explosions 3 and 4 (Fig. 6) appear to be much grainier and

have much lower temperature values despite having similar ambient temperature. This may partially be the result of the higher humidity and an increasingly poor atmospheric path length conditions compared with the first two explosions. Thermal data for the last two explosions (5 and 6) were collected during periods of high humidity (>90%), with condensation occurring on the camera lens itself, giving completely unreliable temperature values. Regardless of the deteriorating conditions, the relative (temporal and spatial) patterns observed around the times of all explosions are repeatable and remain valid for the purpose of observing the dynamics of the thermal structure of the vent surface.

The generation and evolution of the ash plumes produced by the explosions are displayed as FLIR image sequences in Figs. 5 and 6. Note the temperature scale adjustment between sequences in the two figures to accommodate lower apparent temperatures of the latter two explosions. Plumes emitted by the explosions were all initiated by emission across the inner annulus. A few seconds later the main plume emission followed from the outer annulus. In the case of explosion 4, the initial emission from the inner

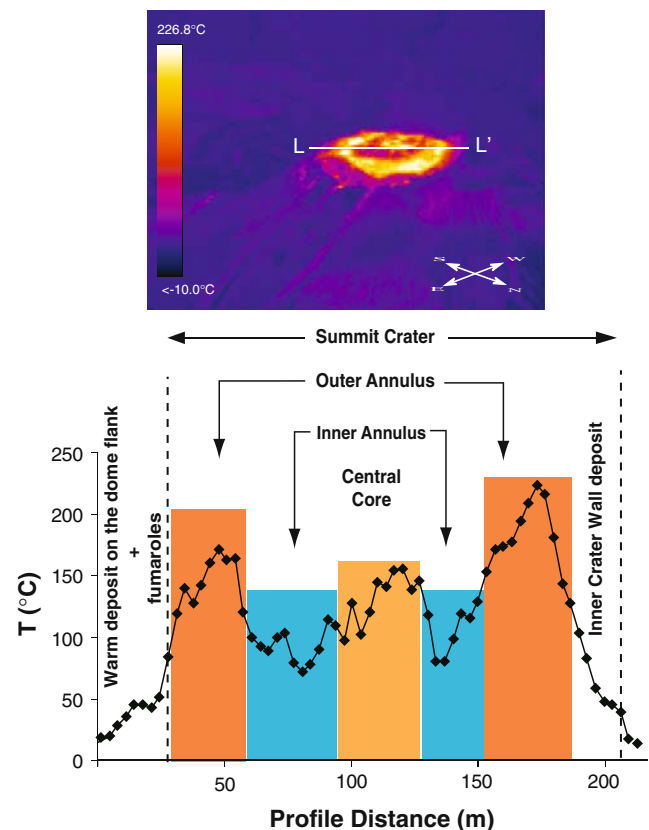
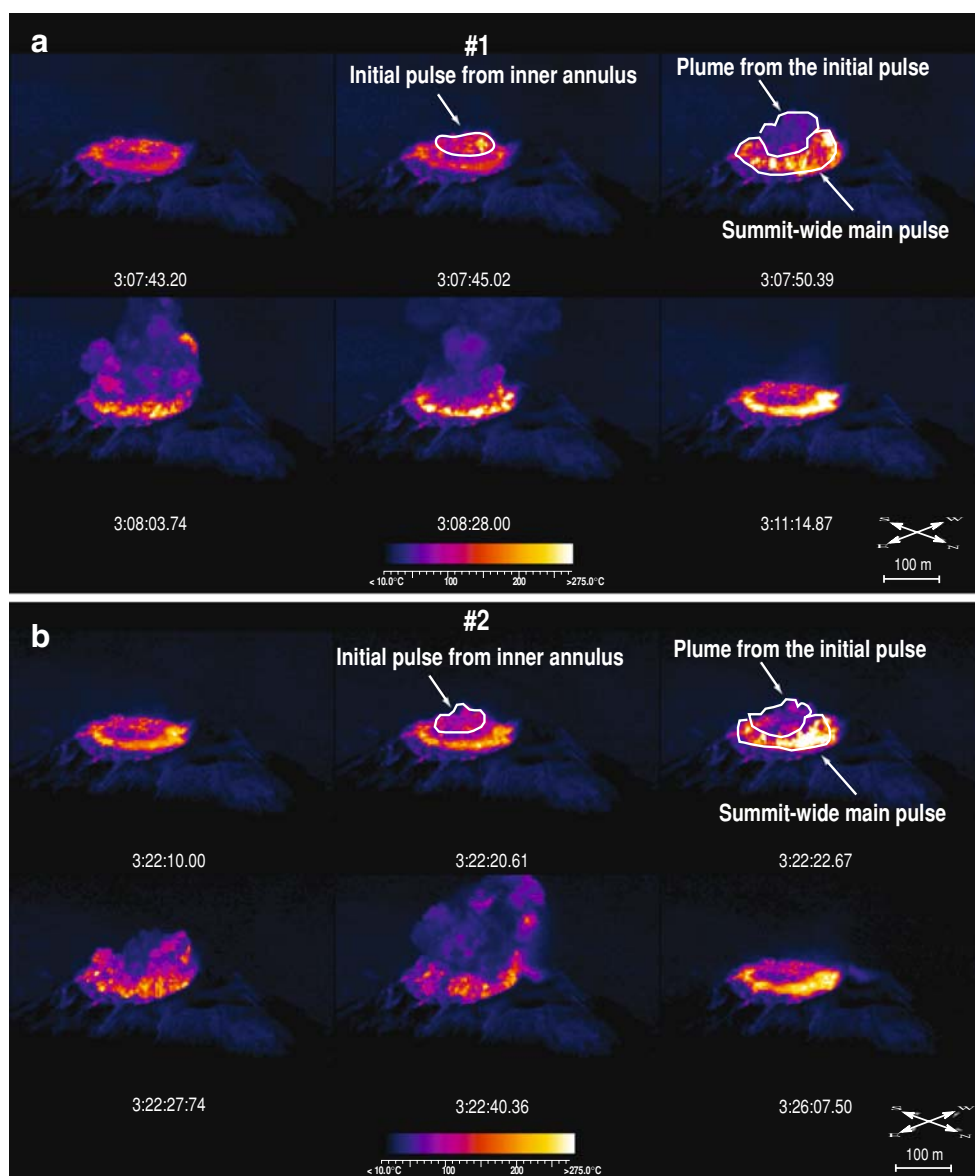


Fig. 4 Temperature profile (L–L') taken across the summit crater immediately before the first explosion, showing the three thermal zones of the vent. Elevated temperature beyond the right hand portion of the outer annulus represents the inner crater wall, which is blanketed with warm pyroclastic deposit from the ash plume. Warm surface beyond the left edge of the outer annulus comprise warm pyroclastic material and fumaroles

Fig. 5 Series of six FLIR images extracted at different time intervals (as shown by time stamps), during **a** explosion 1 and **b** explosion 2 to illustrate plume emission from initial exit to complete dispersal

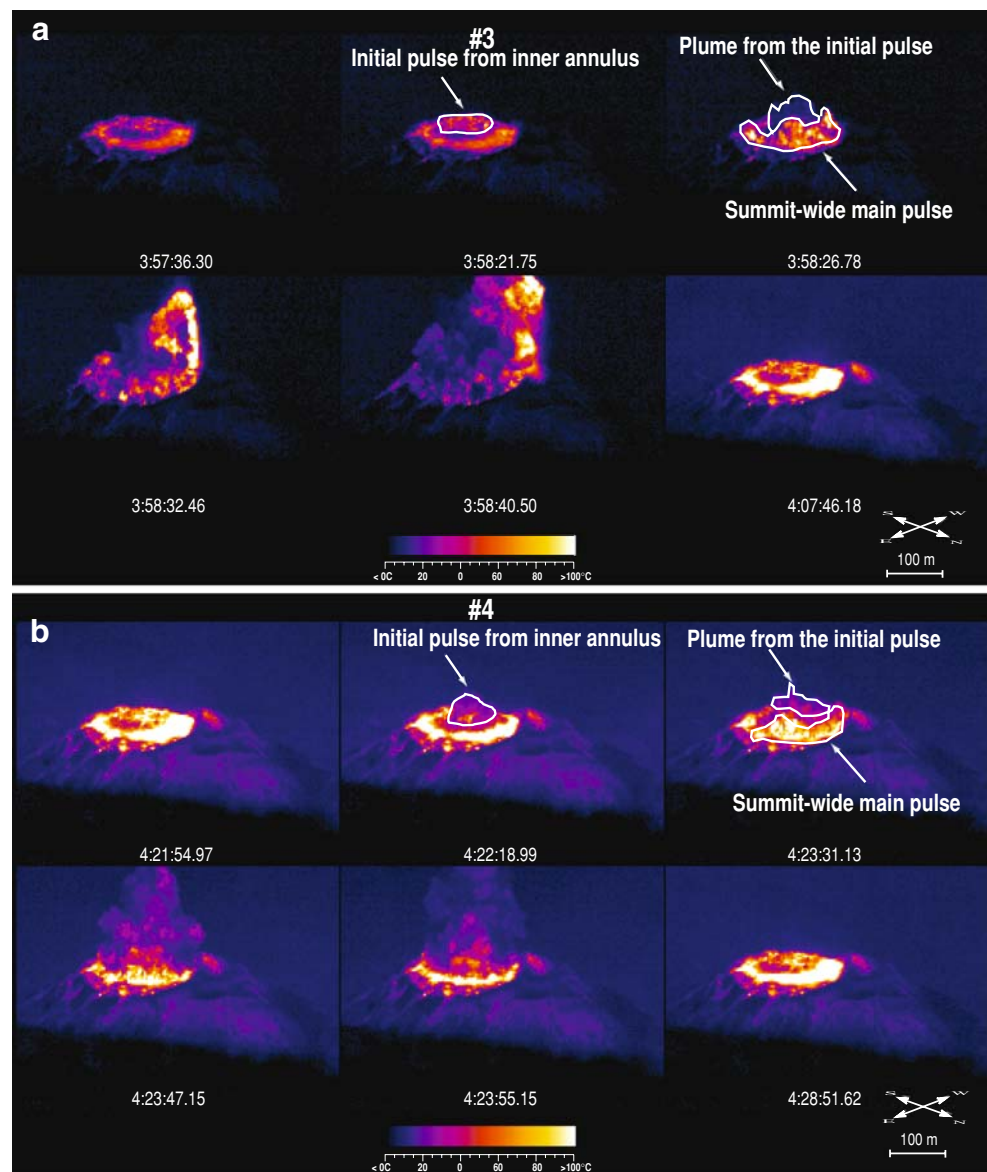


annulus preceded the main plume by at least a minute (Fig. 6b). This ash plume eruption sequence is consistent with previous video-based observations of Bluth and Rose (2004), in which the outward migration of the emission source from the inner to the outer annulus was observed. Explosions 1 and 4 emitted plumes evenly from across the entire the outer annulus, producing cylindrical plumes. Explosions 2 and 3, however, showed most intense and prolonged emission from the right side of the outer annulus, producing non-symmetric plumes and depositing material preferentially on the right hand flank of the dome.

Temperature time series constructed for the duration of an explosion can be used as an alternative way to illustrate the temporal evolution of the plumes generated by the explosions and changes in the vent surface temperature. We extracted two temperature time series for the duration of

explosion 1—this being the explosion imaged under clearest conditions. The first time series involved tracking the maximum temperature recorded from the entire image, and the second tracked the maximum temperature recorded for the summit area only (Fig. 7). We tracked the whole-image maxima to identify any temperature anomalies beyond the summit crater, which should be indicative of elevated temperatures within the plume itself (i.e. the maximum is not at the vent region, but higher in the plume). Masking of the vent by cold ash during the emission may cause maximum temperatures to occur within the plume at some height above the vent itself, which will be missed if only the vent temperature is tracked. The time series shows six temperature peaks corresponding to six different pulses of varying intensity during the emission. The highest temperature at a given time is generally from

Fig. 6 Series of six FLIR images showing plume emission during **a** explosion 3 and **b** explosion 4. Temperature scales are adjusted to account for lower recorded temperatures due to higher relative humidity compared to the first two explosions

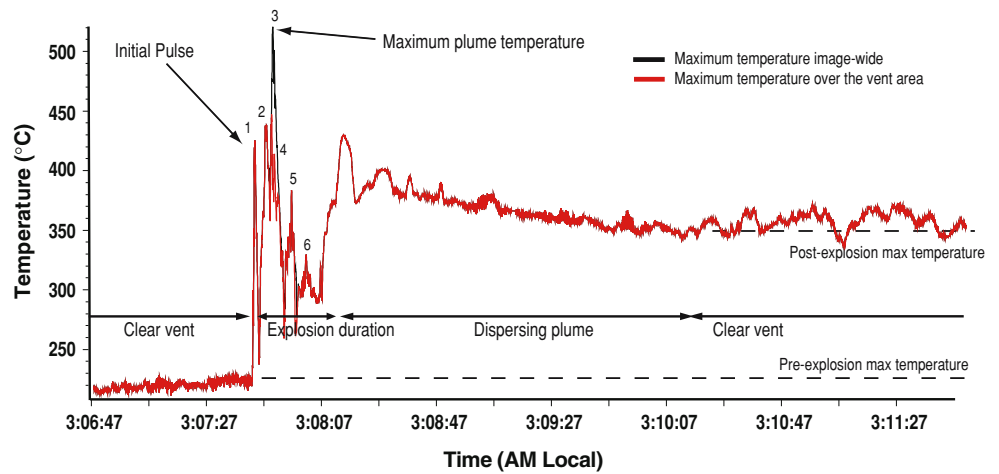


within the summit area, except during the third pulse when maximum temperature is recorded from outside of the summit region (Fig. 7). For explosion 1, the initial plume emission has a maximum temperature of $\sim 400^{\circ}\text{C}$. The maximum recorded temperature (520°C) occurs ~ 15 s after initial emission from a section of the plume at four to six pixels (14–22 m) above the vent. This higher-temperature pulse was emitted from the southwest side of the crater (i.e. on the back right-hand side of the image). This pulse may have had higher exit temperatures at the vent, because the initial emission and early ascent were obscured by cooled ash from the previous pulse. The maximum temperature pulses during the ash emissions are consistently located within this southwest region of the summit for all of the explosions. This region corresponds to the location of the inner annulus discontinuity, where the active block lava

flow exits the summit crater. The explosion 1 temperature time series also shows that the maximum temperature recorded for the vent surface is approximately 175°C higher after the explosion than before it (Fig. 7).

The summit-wide temperature distribution and its temporal evolution are also presented as a series of isotherm maps (Fig. 8). Here we use the thermal images acquired immediately before (column a) and after (column b) each of explosions 1 through 4 to show the changes caused by the explosion. A third temperature map (column c) shows the temperature change for each explosion (post-explosion image minus pre-explosion image). Explosion 1 occurred 14 min into our dataset, and no explosion had occurred during the instrument setup period of 20 min; therefore no explosion had occurred for at-least 34 min. Sahetapy-Engel et al. (2008) observed a maximum repose

Fig. 7 Maximum temperature time series for the duration of explosion 1. *Solid black line* is the maximum temperature recorded from the whole image and the *solid red line* is the maximum temperature recorded from the vent area. For most of the duration of the time series maximum temperature is recorded over the vent area, thus the series overlap one another. Six emission pulses during the explosion can be identified by temperature spikes on the time series



period of ~ 70 min. We thus assume that the pre-explosion thermal structure can represent a stable background state for the summit vent thermal structure, where the surface had largely recovered from disturbance during the previous explosive event. After a half an hour of cooling, the outer annulus can still be clearly identified outlining the margins of the summit crater (Fig. 8a). Outside of this, a cooler rim marks the crater walls. Thermally, the surface of the outer annulus is relatively homogenous at this stage, the temperature mostly being between 100 and 150°C, except for the left-most and right-most portion of the

region, where temperatures are between 150 to 250°C. The inner annulus can also be distinguished by relatively cool temperatures of 50–100°C, just inside the hot zone of the outer annulus. Within the inner annulus, the central core has temperatures of 100–200°C.

Significant temperature changes occur across the outer annulus as the surface was transformed by the explosion (Fig. 8b); with this region showing a change from a relatively homogeneous surface to one marked by several clusters of higher temperatures arranged around the annulus. The temperature of the outer annulus region

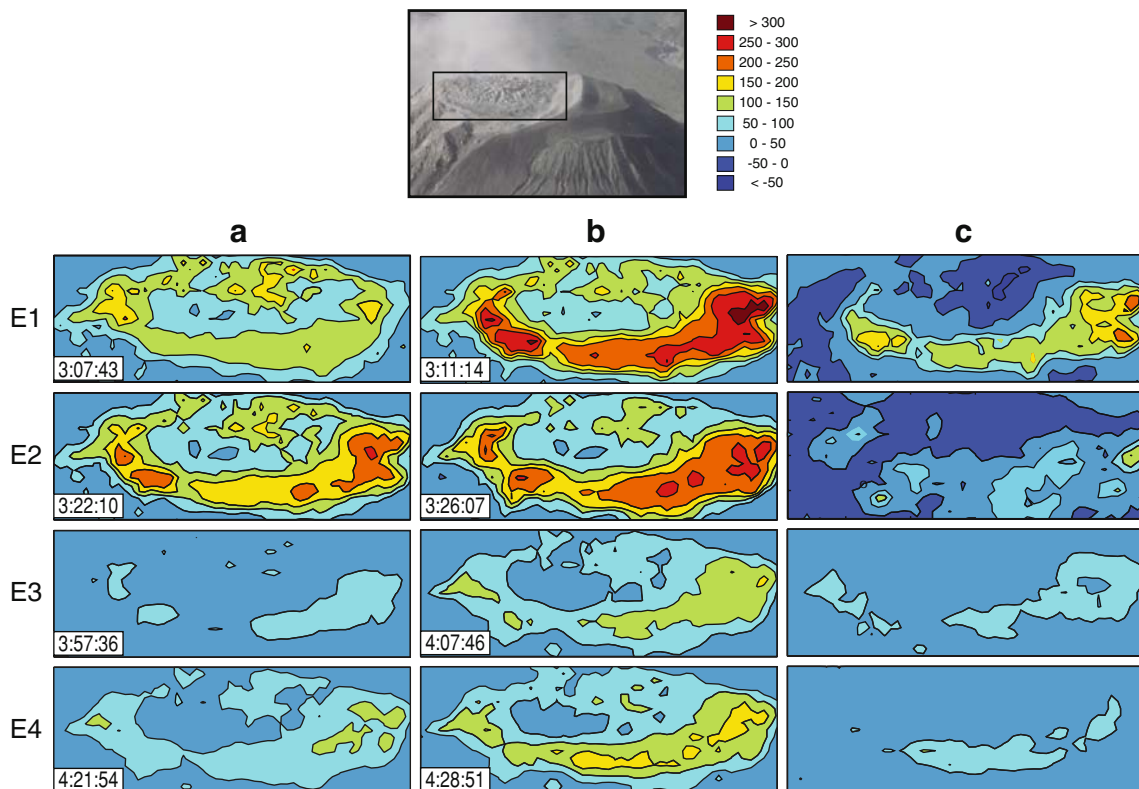


Fig. 8 Temperature maps of Caliente summit for explosions 1 to 4 (E1–E4). Three maps are given covering the zone marked by the black box on the digital photo, where each column gives isotherm maps for **a** before and **b** after each explosion, with **c** giving the temperature change map

generally increased to between 200 and 300°C, with temperatures of greater than 300°C in some of the hotter clusters. The inner annulus, on the other hand, experiences no significant changes in temperature, showing only slight increases at localized areas. The central core shows a general decrease in temperature by about 50°C (Fig. 8c).

Ten minutes elapsed between explosions 1 and 2. Immediately prior to explosion 2, the overall vent surface had not cooled to the state observed prior to explosion 1 (Fig. 8a). The thermal structure across the outer annulus was still quite heterogeneous. The inner annulus was again relatively cool and homogenous, with localized areas of elevated temperature. The central core was also still apparent as a zone of elevated temperature, with a similar temperature level and structure to that observed prior to explosion 1. The thermal structure following explosion 2 shows similar, if slightly less dramatic, changes in temperature to those encountered following explosion 1 (Fig. 8b). Sources of elevated temperature are encountered in the same locations as mapped following explosion 1. We suspect that the locations of these elevated temperature sources mark more permeable fracture zones, allowing for more efficient gas-transfer and heat loss. These zones are likely rooted to pathways extending downwards from the summit vent surface into the upper conduit.

Although the absolute temperatures extracted across the vent area vary as a result of thermal renewal during explosive events and changes in viewing conditions (especially for explosions 3 and 4), the relative thermal structure remains stable through time and between explosions. The assumed stable state of the vent structure, as represented by pre-explosion 1 surface (Fig. 8a, E1), has the outer annulus maintaining higher temperatures than the inner annulus, suggesting higher levels of permeability allowing increased heat flow from below. The resulting vent thermal structure comprises a thermally static inner zone of low heat transfer enclosed by a dynamic, high heat flux outer zone. This structure is consistent with a massive, impermeable central region, bounded by high permeability shear zone, which is interrupted by extrusion of lava on its southwestern side. The stability of this surface configuration with time implies that the sub-surface structures responsible for this surface pattern were also stable across the observation period.

Shallow level conduit structure

Based on the surface thermal characteristics and their response to explosions, we can make some comparison between the different thermal regions and the surface morphology observed from digital photography (Fig. 9). A generalized cartoon summarizing our inferred surface

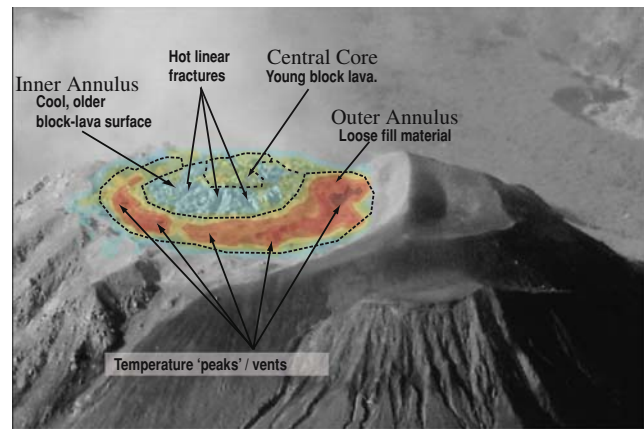


Fig. 9 Thermal map (panel b for explosion 1 of Fig. 8) overlain on a digital photo of the Caliente summit crater showing the relationship between the different thermal regions and morphological features of the summit

structure along with two cross-sections across the summit crater is given in Fig. 10. The outer annulus corresponds to a region that appears to be depressed and contains a series of smaller pits (Fig. 9). Compared with other regions of the summit crater, the surface of this depression is comprised of what appears to be finer material. These pits have been documented by previous workers (Bluth and Rose 2004; Sahetapy-Engel et al. 2004) and were interpreted as individual vents. The location of these vents is consistent with the location of the thermally elevated zones observed after each explosion, suggesting that they host much of the venting of hot gas and ash.

The inner cold annulus is located over a portion of the crater occupied by a blocky surface that appears to slope away from the center of the vent. Hot fractures dissecting the inner annulus, observed in the thermal data, can also be distinguished in the digital photo. Given its relatively cool temperatures and structure, the inner annulus most likely represents the surface of a thick, relatively cool lava crust. The observed fractures radiating at higher temperatures suggest that higher temperature lava resides just beneath this carapace; and suggests doming above an ascending plug of hot lava. The central hot region appears to be composed of a relatively smooth surface. The temperature of this region falls in the same range as that of the fractures in the inner annulus. We suggest that the central hot region thus represents surface exposure of active and most recent lava which is extruded to feed the active block lava flow that exits the vent to the SW. This would suggest lava upwelling over the central core, before flowing out of the crater to the SW. This central upwelling of younger lava may have initially broken up an older lava unit of the inner annulus, producing the observed radial fractures. Maximum plume emission temperatures are observed from the region of lava overspill and further support the presence of active

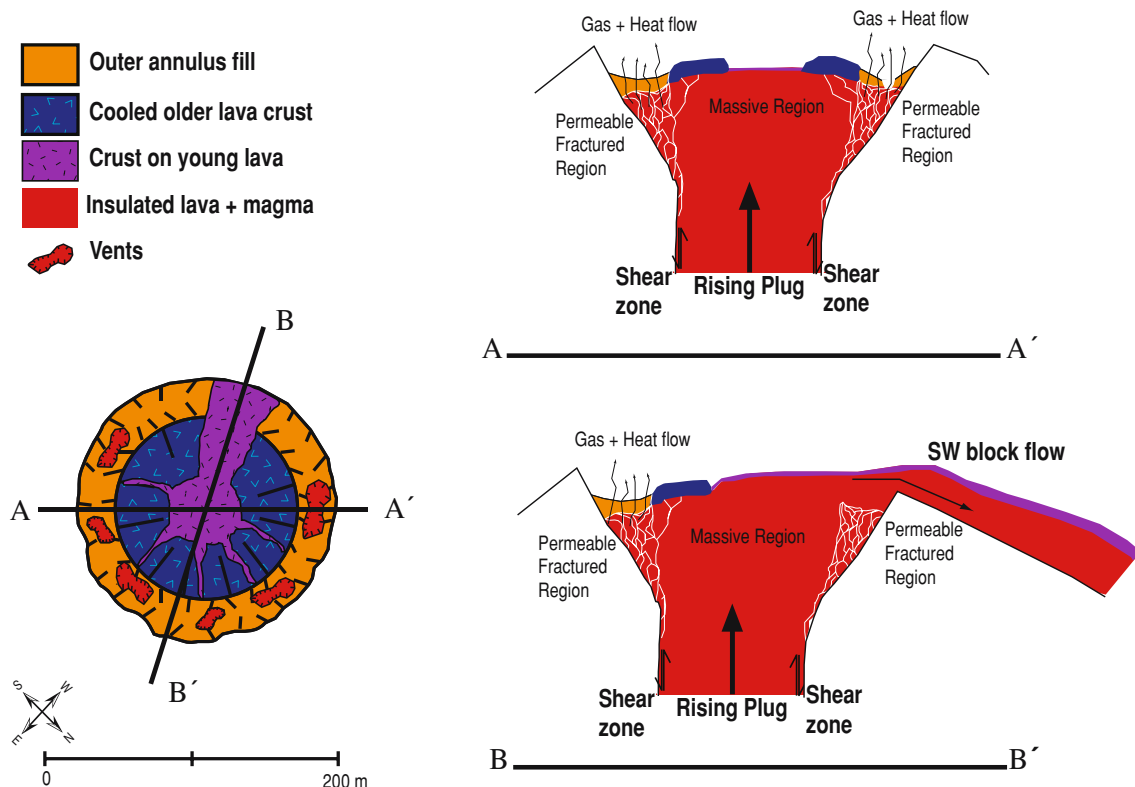


Fig. 10 Cartoon showing the summit crater and shallow conduit structure in plan view and cross-section. Total width of the crater is approximately 180 m and cross-sections are not to vertical scale. Conduit width is also not known, and is likely narrower than the vent

lava extrusion in this portion of the vent, where pulverization of the fresh lava in the shallow conduit would contribute to the higher temperatures.

The temperature of the outer annulus fill is significantly higher than that of the exposed lava surfaces, most likely due to the higher permeability of the fill material to allow preferential flow of heat and gas through this region. The significant increase in temperature of the outer annulus during an explosion can be explained by deposition of materials ejected during the explosion. However, we observed that pyroclastic materials deposited on the lava surface of the cold inner annulus only accounts for a $\sim 50^\circ\text{C}$ increase in temperature, compared to the observed temperature increase of $200\text{--}300^\circ\text{C}$ in the outer annulus. We suggest that the large increase in temperature of the outer annulus is due to an increase in the permeability of this zone following an explosion. Subsequent cooling of this zone, as permeability decreases due to re-annealing of previously opened fractures, is thus related to the relatively fractured nature of the underlying structure of the outer annulus. Thus this zone is able to maintain its relatively high temperature. The central lava region, with its stable gas and heat flux conditions around an explosion, is somewhat more impermeable. This structure is consistent

width. However, the upper section of the conduit may be quite wide where Tanaka et al. (2007) imaged the conduit size of the Showa-Shinzan lava dome (Japan) using cosmic-ray muons and obtained a diameter of $\sim 102\text{ m} \pm 15\text{ m}$ for the upper-most section

with a massive, impermeable, central lava plug surrounded by a highly fractured marginal shear zone.

Surface Heat Flux The calibrated thermal data obtained under good conditions allow us to estimate the proportion of heat loss associated with each thermal zone identified across the vent area. We assume that cooling and crystallization of magma ascending the conduit to feed the explosive emissions and lava flow provide the heat then lost at the summit vent. The magma, on arriving in the vent area, is exposed at the surface in the hot central core area, the fractures within the inner annulus, and the intra-crater portion of the SW block lava flow. Dissipation of heat from this magma influx is assumed to occur via radiative (q_{rad}) and convective heat transfer (q_{conv}) into the atmosphere. Lateral heat transfer via conduction through conduit walls may also contribute to the overall heat budget but is not quantifiable from this study. Given the FLIR-derived surface temperature (T_{surf}) and measured ambient temperature (T_{air} , Table 1), the heat flux density q_{rad} (in $\text{J s}^{-1} \text{m}^{-2}$) can be calculated using the Stefan-Boltzmann equation:

$$q_{\text{rad}} = \varepsilon\sigma(T_{\text{surf}}^4 - T_{\text{air}}^4) \quad (1)$$

where ε is the surface emissivity (0.9) and σ is the Stefan Boltzmann constant ($5.67 \times 10^{-8} \text{ J K}^{-4} \text{ m}^{-2} \text{ s}^{-1}$). Convective heat loss can be calculated as free convection (q_{free}) in cases where there is no wind or forced convection (q_{forced}) during windy conditions. We did not collect wind measurements at this time, but conditions were calm (winds were light to minimal). Thus, we estimate free convective heat flux density (q_{free}). Free convection can be calculated from:

$$q_{\text{free}} = h_c(T_{\text{surf}} - T_{\text{air}}) \quad (2)$$

in which h_c is the free convection heat transfer coefficient calculated for each of the thermal zones, where we obtain h_c of 8.4–11.4, 6.2–7.6 and 7.7–9.5 $\text{J s}^{-1} \text{ m}^{-2} \text{ K}^{-1}$, for the outer annulus, inner annulus and central core, respectively (see Appendix).

We carry out heat flux density measurements for each of the thermal components identified within the summit crater (Fig. 11). The first component of the thermal model is the young lava component, which has surface temperatures of 100–200°C. This component occupies an 830 m^2 area extending across the hot central zone, the five fractures within the inner annulus (total area of 437 m^2), and the intra-crater portion of the SW-flank lava flow which dissects both the inner and the outer annulus (13 m-wide with a total surface area of 455 m^2). This gives a total area for this young lava thermal component of 1,722 m^2 . The second thermal component occupies the inner annulus zone which is mostly comprised of the cooled crusts of older lava at temperatures of 40–80°C. The total surface area of this region (minus the fractures and the SW lava flow) is 6,530 m^2 . The third component occupies the outer annulus which is filled with loose material at 150–400°C and has a total surface area (minus the SW lava flow) of 12,904 m^2 . Multiplying area by heat flux density, allows the total heat

flux or power loss from each zone (in J s^{-1}) to be calculated.

The results of the calculations are summarized in Table 2. The minimum and maximum limits of calculated heat fluxes are dictated by the minimum and maximum range of temperatures used for each region. Maximum heat flux density occurs at the outer annulus with the inner annulus, which is comprised of cool lava crust of older lava, having the lowest heat flux densities. Young lava surfaces (central core + fractures + lava flow) have values intermediate between those of the outer and inner annulus (Table 2). Total power loss ($Q_{\text{surf}} = Q_{\text{rad}} + Q_{\text{free}}$) from the summit vent (in MJ s^{-1}) is dominated by the outer annulus fill, where Q_{surf} ranges between 31–176 MJ s^{-1} (Table 2). This region accounts for 86–93% of the total power loss from the entire vent. Despite its low temperature, the inner annulus (old lava) contributes nearly the same amount to the overall power loss (2.41–7.07 MJ s^{-1} or 8–5% of the total) as the much higher temperature zones of the fractures, inner core and discontinuity (2.68–6.92 MJ s^{-1}). This is a result of the January 2005 surface configuration, wherein the young lava surface zones exposed at the core, fractures and discontinuity comprised the smallest fractional area of the summit crater (Table 2).

Surface crust and depth to magmatic temperatures

The temperatures measured for the young lava surface component at the summit (100–200°C) is significantly lower than the expected eruption temperature of dacite (800–1100°C, Cas and Wright 1987). Sahetapy-Engel et al. (2004) applied a two-component thermal model to hyper-spectral data and found that the summit surface comprised a 120–250°C cold component broken-up by very small fractures radiating at near eruptive temperatures of ~950°C. The temperature range for the cold component obtained by Sahetapy-Engel

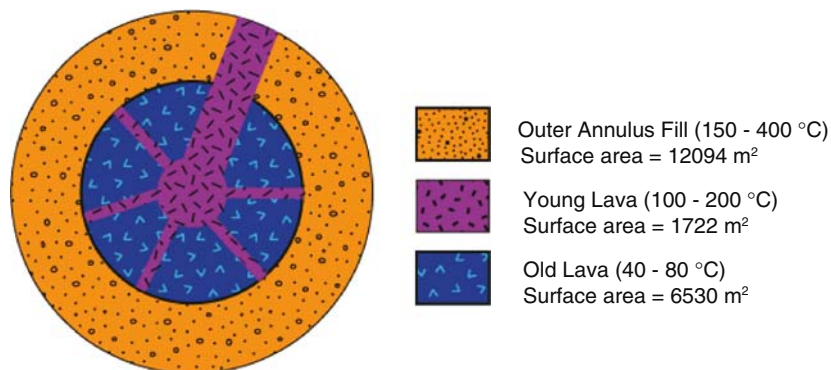


Fig. 11 A generalized three-component model of the vent thermal structure, used to estimate surface heat flux density and power loss. Temperature range and total surface area of each component are listed. Dimensions of each component are assumed from widths measured

along the profile taken across the summit vent and extrapolated for the whole summit. The young lava surface is comprised of the central core, the fractures in the inner annulus and the active block lava flow that exits the vent across its SW rim

Table 2 Calculated heat flux densities (q_{rad} and q_{free} in $\text{J s}^{-1} \text{m}^{-2}$) and power loss (Q_{rad} , Q_{free} and Q_{surf} in MJ s^{-1}) for each thermal zone within the summit crater for the observed minimum and maximum thermal-image-derived temperatures (T_{surf})

	Core, fractures discontinuity (young lava)		Cold inner annulus (old lava)		Outer annulus fill		Total	
	Min	Max	Min	Max	Min	Max	Min	max
Area (m^2)	1,722		6,530		12,094		20,346	
T_{surf} ($^{\circ}\text{C}$)	100	200	40	80	150	400		
q_{rad} ($\times 10^3 \text{ J s}^{-1} \text{m}^{-2}$)	0.68	2.25	0.19	0.49	1.33	10.1	2.20	12.9
q_{free} ($\times 10^3 \text{ J s}^{-1} \text{m}^{-2}$)	0.72	1.86	0.22	0.57	1.23	4.49	2.17	6.92
q_{surf} ($\times 10^3 \text{ J s}^{-1} \text{m}^{-2}$)	1.40	4.11	0.41	1.06	2.56	14.6	4.38	19.8
Q_{rad} (MJ s^{-1})	1.17	3.87	1.24	3.20	16.1	122	18.5	129
Q_{free} (MJ s^{-1})	1.24	3.20	1.44	3.72	14.9	54.3	17.6	61.2
Q_{surf} (MJ s^{-1})	2.41	7.08	2.68	6.92	31	176	36.1	190

et al. (2004) is consistent with our measurements given here, suggesting that our measurements are dominated by the same cold crusted surface as identified in 2002 by Sahetapy-Engel et al. (2004). The FLIR failed to resolve the higher temperature surface due to the limited the sub-pixel extent of the high temperature cracks. The relatively low temperature compared to the eruptive temperature can be attributed to the initial rapid cooling of extruded lava, forming an outer crust that insulates the underlying material at magmatic temperature. A similar phenomenon is observed on the block-lava that is fed by this vent, where an exceedingly cool (near-ambient) crust insulates the flow core (Harris et al. 2002, 2004). In fact, these at-vent crust temperatures match the near-vent surface maxima obtained for the lava flow surfaces measured during 2000–2002 by Harris et al. (2004) of $\sim 150^{\circ}\text{C}$.

From the heat flux density estimates we can estimate the depth to the 950°C isotherm for the lava regions of the summit using Fourier's Law. Using this approach, depth to the 950°C isotherm may be viewed as roughly equivalent to the thickness (δ) of the outer crust on any lava body (e.g. Oppenheimer 1991, Harris et al. 2002). The main assumption is that the rate of heat loss at the surface is equal to the rate of heat conducted from the magmatic surface upwards through an overlying boundary layer, so that,

$$q_{\text{cond}} = k \frac{(T_{\text{core}} - T_{\text{surf}})}{\delta} \quad (3)$$

where k is the thermal conductivity of the surface, assumed for Santiaguito rocks to be $2 \pm 1 \text{ W m}^{-1} \text{ K}^{-1}$ (Robertson and Peck 1974), T_{core} is the core (magmatic) temperature and T_{surf} is the surface temperature. T_{core} can be assumed to be equivalent to the eruption temperature ($T_{\text{erupt}} = 950^{\circ}\text{C}$ = maximum of Sahetapy-Engel et al. 2004). For the young lava surface of the core, fracture and discontinuity zones where T_{surf} is in the range 100 – 200°C , the depth to the

magmatic layer (or the crust thickness) ranges from 0.3 to 2 m. Thickness of the old extruded lava exposed across the inner annulus (at 40 – 80°C) ranges from 1.5 – 4.3 m.

We apply this method to calculate the depth to magmatic temperature along the L–L' cross-section (Fig. 4) of the summit crater and use pre-explosion temperature profile from explosion 1, which is assumed to be the stable state of the summit crater. Across this profile (Fig. 12), the thickness of the carapace on the older lava that comprises the inner annulus ranges from 1 to 3 m. The crust thickness of the young lava of the inner annulus is much lower at 0.3 to 1.5 m. The thickness of the fill layer of the outer annulus was not estimated given the uncertainty in the particle size and the porosity of this granular deposit. This complicates the calculation of total heat conducted through deposit;

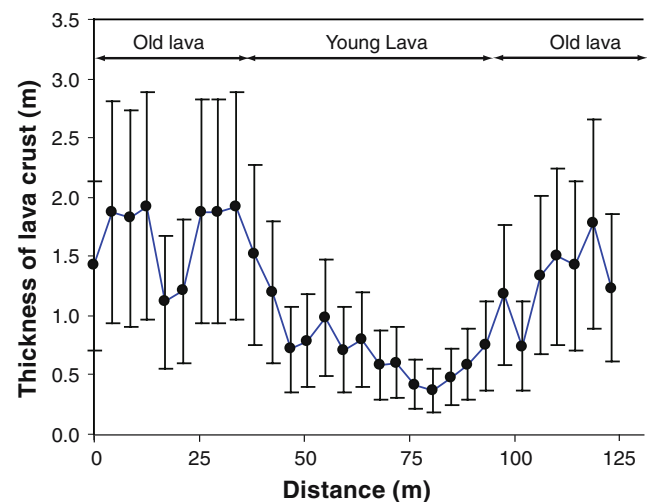


Fig. 12 Estimated crust thickness of the old lava (inner annulus) and the young lava (central core) regions within the vent using a simple conduction model. The temperature profile used for calculation is taken immediately preceding explosion 1. The error bars represent the uncertainty in the thermal conductivity value used in the calculations

invalidating the application of Eq. 3 to this region given that heat is likely transmitted through this zone by permeable convection.

Conclusions

Following Gonnerman and Manga (2003), intermittent explosions and associated vertical ash plumes at Santiaguito have been attributed as resulting from shear-induced fragmentation along the conduit walls (Bluth and Rose 2004; Sahetapy-Engel et al. 2008). Within this model, the outer annulus is a surface expression of an annular fracture zone at the margins of the broadly cylindrical central plug. Sahetapy-Engel et al. (2008) further suggested that fragmentation occurs at depths between 100–500 m below the vent, with the pyroclastic material generated propagating up the fracture zone at the conduit boundary, to exit across the outer annulus. As such, the conduit boundary provides a logical pathway, intermittently ‘cleaned out’ by the explosions and through which heat, gas and solid material from the shallow-surface magma column can escape. This is consistent with our observation that the outer annulus is stable in space and time and is the most productive heat generator at the summit crater.

This sub-surface structure results in a plug-like feature within the crater, comprising a central core of lava which spills out of the crater to feed flank lava flows, surrounded by the hot outer annulus that marks the top of the marginal shear zones surrounding this plug. Interestingly, this thermal and structural configuration means that intermittent explosions result in elevated temperatures mainly at the outer annulus but not across the central core or plug. Thermal renewal is only effective at the outer annulus, where heat and mass flow is more efficient by virtue of the high permeability of this marginal fracture zone when compared with the central plug. This in turn drives the wide range of total summit power output observed at Caliente vent (35–187 MJ s⁻¹), where heat loss is most efficient (highest) at the fracture zones and reduced across the plug.

Acknowledgments We would like to thank Robert Wright, Oto Matias, Rudiger Wolf and Lizzette Rodriguez for their assistance in collecting the data. We also would like to thank Bill Rose, INSIVUMEH and the staff at the Santa Maria Volcano Observatory for providing logistical assistance and support. Reviews by Eliza Calder, Bill Rose, Luke Flynn, Bruce Houghton, Matthew McGranaghan and Robert Wright greatly improved this manuscript. Funding for this study was provided by a NASA Earth Systems Science Fellowship, NSF Grant EAR-0207734 and NASA grant NNG04GO64G. FLIR was purchased using an NSF equipment grant (An Equipment Proposal: Volcanic Conduit Dynamics Observed Through Forward Looking Infrared Radiometry; PI: Jon Dehn, University of Alaska, Fairbanks) and HIGP funds.

Appendix

Convective heat transfer coefficient

Free-convection heat transfer coefficient (h_c) is calculated following Holman (1992) using the Nusselt Number (Nu),

$$\text{Nu} = \frac{h_c H}{k_{\text{air}}}$$

where H is the thickness of the hot fluid overlying the surface (in m) and k is the thermal conductivity of the overlying air (J s⁻¹ m⁻¹ K⁻¹). For free convection, cooling can be calculated using the Rayleigh number (Ra) which is obtained from the Nusselt Number in

$$\text{Nu} = 0.16\text{Ra}^{1/3}$$

Ra is the product of the Grashof number (Gr), which is the ratio of buoyancy forces to viscous forces, and the Prandtl number (Pr), which is the ratio of momentum and thermal (i.e. $\text{Ra} = \text{Gr Pr}$). The Grashof number can be calculated by,

$$\text{Gr} = \left[\frac{g\beta(T_{\text{surface}} - T_{\text{ambient}})H^3}{\nu^2} \right]$$

Where g is gravitational acceleration (9.8 m s⁻²), β is the inverse of the mean temperature (T_{mean}) of the overlying thermal boundary layer [$T_{\text{mean}} = (T_{\text{surface}} + T_{\text{ambient}})/2$], and ν is the kinematic viscosity of the overlying fluid (m² s⁻¹). The Prandtl Number is given by,

$$\text{Pr} = \frac{\nu}{\alpha}$$

where α is thermal diffusivity (m² s⁻¹). This sequence of equations is used to calculate h_c on a pixel-by-pixel basis using the pixel temperature for T_{surface} and the measured atmospheric air temperature for T_{ambient} .

References

- Ball M, Pinkerton H (2006) Factors affecting the accuracy of thermal imaging cameras in volcanology. *J Volcanol Geotherm Res* 111: b11203 DOI 1029/2005JB003829
- Birnie RW (1973) Infra-red radiation thermometry of Guatemala volcanoes. *Bull Volcanol* 37:1–36
- Bluth GJS, Rose WI (2004) Observations of eruptive activity at Santiaguito volcano, Guatemala. *J Volcanol Geotherm Res* 136:297–302
- Cas RAF, Wright JV (1987) Volcanic successions, modern and ancient. Allen & Unwin Ltd., London
- Gonnerman HM, Manga M (2003) Explosive volcanism may not be an inevitable consequence of magma fragmentation. *Nature* 426:432–435
- Harris AJL, Flynn LP, Matias O, Rose WI (2002) The thermal stealth flows of Santiaguito: implications for the cooling and emplace-

- ment of dacitic block lava flows. *Geol Soc Am Bull* 114:533–546
- Harris AJL, Rose WI, Flynn LP (2003) Temporal trends in lava dome extrusion at Santiaguito 1922–2000. *Bull Volcanol* 65:77–89
- Harris AJL, Flynn LP, Matias O, Rose WI, Cornejo J (2004) The evolution of an active silicic lava flow field: An ETM + perspective. *J Volcanol Geotherm Res* 135:147–168
- Holman JP (1992) Heat transfer. McGraw-Hill, London
- Johnson JB, Harris AJL, Sahetapy-Engel S, Wolf RE, Rose WI (2004) Explosion dynamics of pyroclastic eruptions at Santiaguito volcano. *Geophys Res Lett* 31:L06610 DOI [10.1029/2003GL019079](https://doi.org/10.1029/2003GL019079)
- Oppenheimer C (1991) Lava flow cooling estimated from Landsat Thematic Mapper infrared data - The Lonquimay eruption (Chile, 1989). *J Geophys Res* 96:21865–21878
- Robertson EC, Peck DL (1974) Thermal conductivity of vesicular basalt from Hawaii. *J Geophys Res* 79:4875–4888
- Rose WI (1972) Notes on the 1902 eruption of Santa Maria Volcano, Guatemala. *Bull Volcanol* 36:29–45
- Rose WI (1987) Volcanic activity at Santiaguito volcano 1976–1984. *Geol Soc Am Spec Pap* 212:17–27
- Sahetapy-Engel ST, Flynn LP, Harris AJL, Bluth GJL, Rose WI, Matias O (2004) Surface temperature and spectral measurements at Santiaguito lava dome, Guatemala. *Geophys Res Lett* 31:L19610 DOI [10.1029/2004GL020683](https://doi.org/10.1029/2004GL020683)
- Sahetapy-Engel ST, Harris AJL, Marchetti E (2008) Thermal, seismic and infrasound observations of persistent explosive activity and conduit dynamics at Santiaguito lava dome, Guatemala. *J Volcanol Geotherm Res*. DOI [10.1016/j.physletb.2003.10.071](https://doi.org/10.1016/j.physletb.2003.10.071) (in press)
- Sapper K (1926) Die Vulkanische Tätigkeit in Mittelamerika im 20 Jahrhundert. *Zeitschrift für Vulkanologie* 9:156
- Stoiber RE, Rose WI (1969) Recent volcanic and fumarolic activity at Santiaguito Volcano, Guatemala. *Bull Volcanol* 33:475–502
- Tanaka HKM, Nakano T, Takahashi S, Yoshida J, Ohshima H, Maekawa T, Watanabe H, Niwa K (2007) Imaging the conduit size of the dome with cosmic-ray muons: The structure beneath Showa-Shinzan Lava Dome, Japan. *Geophys Res Lett* 34:L22311 DOI [10.1029/2007GL031389](https://doi.org/10.1029/2007GL031389)
- Williams SN, Self S (1983) The October 1902 Plinian eruption of Santa Maria volcano, Guatemala. *J Volcanol Geotherm Res* 16:33–56